

Helium behaviour in implanted boron carbide

Vianney Motte^{1,4*}, Dominique Gosset¹, Sandrine Miro², Sylvie Doriot¹, Suzy Surblé³, and Nathalie Moncoffre⁴

¹ CEA Saclay, DEN-DANS-DMN-SRMA-LA2M, 91191 Gif-sur-Yvette cedex, France

² CEA Saclay, DEN-DANS-DMN-SRMP-JANNuS, 91191 Gif-sur-Yvette cedex, France

³ CEA Saclay, DSM-IRAMIS-LEEL, 91191 Gif-sur-Yvette cedex, France

⁴ CNRS-IN2P3, IPNL, Université Lyon 1, 69622 Villeurbanne cedex, France

Received: 30 April 2015 / Received in final form: 24 September 2015 / Accepted: 5 November 2015

Published online: 16 December 2015

Abstract. When boron carbide is used as a neutron absorber in nuclear power plants, large quantities of helium are produced. To simulate the gas behaviour, helium implantations were carried out in boron carbide. The samples were then annealed up to 1500 °C in order to observe the influence of temperature and duration of annealing. The determination of the helium diffusion coefficient was carried out using the $^3\text{He}(d,p)^4\text{He}$ nuclear reaction (NRA method). From the evolution of the width of implanted ^3He helium profiles (fluence $1 \times 10^{15}/\text{cm}^2$, 3 MeV corresponding to a maximum helium concentration of about $10^{20}/\text{cm}^3$) as a function of annealing temperatures, an Arrhenius diagram was plotted and an apparent diffusion coefficient was deduced ($E_a = 0.52 \pm 0.11$ eV/atom). The dynamic of helium clusters was observed by transmission electron microscopy (TEM) of samples implanted with $1.5 \times 10^{16}/\text{cm}^2$, 2.8 to 3 MeV ^4He ions, leading to an implanted slab about $1 \mu\text{m}$ wide with a maximum helium concentration of about $10^{21}/\text{cm}^3$. After annealing at 900 °C and 1100 °C, small (5–20 nm) flat oriented bubbles appeared in the grain, then at the grain boundaries. At 1500 °C, due to long-range diffusion, intra-granular bubbles were no longer observed; helium segregates at the grain boundaries, either as bubbles or inducing grain boundaries opening.

1 Introduction

With a high neutron absorption efficiency, a good availability and a relatively low cost, boron carbide is used in almost all types of nuclear power plants. It is also widely used as grinding tools or armors, thanks to its mechanical properties: boron carbide is a light (2.52 g/cm^3 for a fully dense material) super-hard (HV ~ 40 GPa) ceramic [1,2]. It has a high stiffness (Young modulus ~ 450 GPa) and a high strength (~ 450 MPa) but is brittle ($K_{IC} \sim 6 \text{ MPa}\sqrt{\text{m}}$). It is a semiconductor material with a thermal conductivity varying as $1/T$, about $30 \text{ W/m}\cdot\text{K}$ at room temperature. Those electrical and thermo-mechanical properties come from the interatomic bonding, which is mainly covalent. But its weak thermo-mechanical properties lead to early damage and short life-cycle when used as a neutron absorber.

The crystalline structure of boron carbide, shown in Figure 1, is now known [1–4] as rhombohedral (most often represented in a hexagonal frame). At the carbon-rich limit, the composition is very close to B_4C . The unit cell is built with a central chain, mainly C-B-C, and 8 icosahedra mainly constituted of B_{11}C situated at the corners, giving

the general formula B_4C , which is one of all the polytypes of the boron carbide phase (from $\sim\text{B}_4\text{C}$ to B_{10}C).

Boron carbide has a high atomic density, leading to a boron content of about $10^{23}/\text{cm}^3$. Boron is naturally composed of ^{10}B and ^{11}B isotopes with a natural concentration of

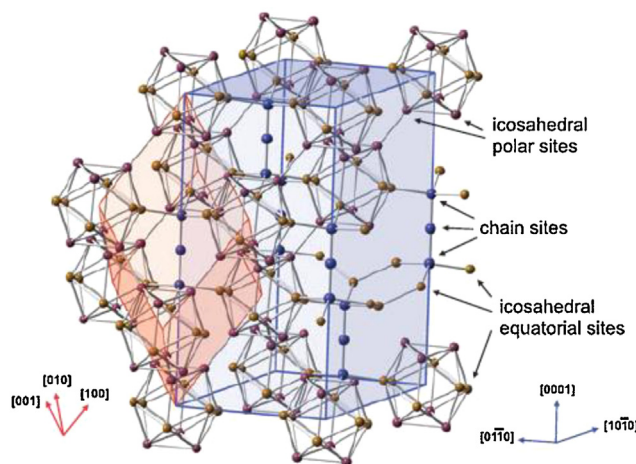


Fig. 1. Cell structure of boron carbide B_4C (from Ref. [1]).

* e-mail: vianney.motte@cea.fr

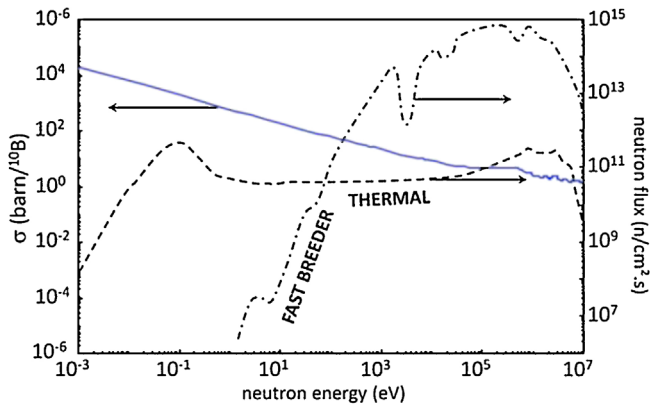


Fig. 2. In blue solid line: neutron absorption cross-section for the ^{10}B isotope (from Ref. [5]), superimposed to the neutron energy distribution (in black) in a pressurised water (- - thermal) and a fast neutron (- · - fast breeder) reactor (from Ref. [6]).

~ 20 at.% ^{10}B , which can be modified from 1 to 99 at.% depending on the application. The boron-10 isotope is a very efficient neutron absorber because of its high neutron absorption cross-section as shown in Figure 2.

As a material used in nuclear plants, many studies were conducted for a better understanding of the B_4C behaviour under irradiation. Two main phenomena happen in the reactors: atomic displacements leading to high point defects concentration, for which structural consequences are actually not well known (possibly amorphisation, at least at low temperature); and helium production that leads to damage in the micro-structural stability.

Amorphisation in boron carbide under irradiation has been observed with light ions at low [7] or high [8] temperatures. Recent studies [9] have shown amorphisation under slow, heavy ion irradiation, for which most of the damage is in the ballistic regime: at high damage ($4 \times 10^{15}/\text{cm}^2$ Au 4 MeV, about 2 to 4 dpa), amorphisation was partial and heterogeneous in the damaged front zone, with the formation of nanometre-scale amorphous zones, and fully amorphous in the gold implantation zone, as shown in Figure 3.

Helium production arises from neutron capture by the $^{10}\text{B}(n,\alpha)^7\text{Li}$ reaction, which is highly exothermic (about 2.6 MeV per neutron capture). Helium accumulates in flat, high pressure and parallel bubbles (mainly parallel to the (111) planes [10–13] and also to the (100) and (110) planes [12–15] of the rhombohedral structure). In fast neutron reactors, the combination of heat release and helium production induces strong radial thermal gradients and extensive cracking of the absorber pellets [4,16,17] as shown in Figure 4.

The first steps of the formation of the helium clusters and the diffusion of the gas are not well known. In this context, we have launched a program aiming to study the dynamics of helium in irradiated boron carbide. Here, we present preliminary results about these two topics. This work is part of a systematic study of the behaviour of the gases in boron carbide used as a neutron absorber, aiming at a better description of the evolution of the material under neutron irradiation.

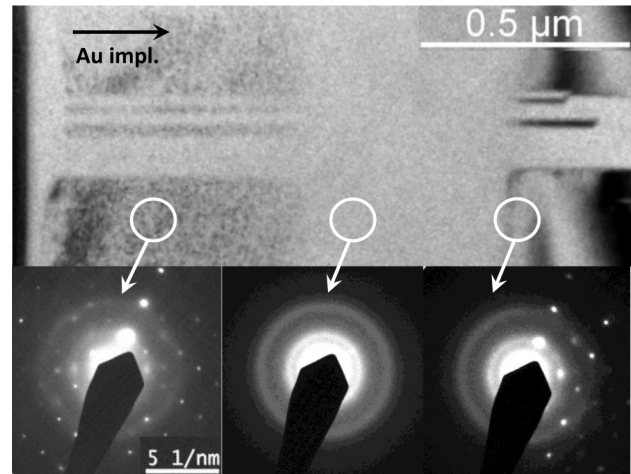


Fig. 3. TEM pictures of B_4C irradiated at $4 \times 10^{15}/\text{cm}^2$ 4 MeV Au ions. An amorphous zone appears in the (centre) implanted zone. Partial amorphisation was observed in the (left) front, damaged zone. Diffraction pictures: (left) at the middle of the speckled front zone; (centre) at the middle of the amorphous zone; (right) at the right amorphous-crystalline boundary (from Ref. [9]).

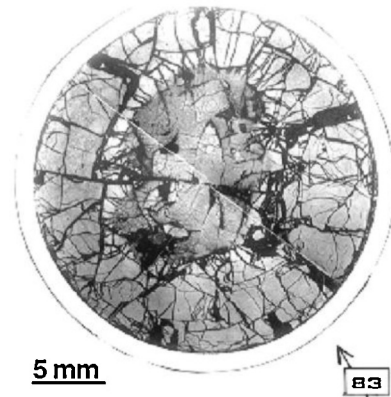


Fig. 4. B_4C pellets (from Ref. [4]) irradiated in the French LMFBR Phenix. 1.2×10^{22} capt./ cm^3 (about 12 at.% total boron).

2 Experiments

In order to overcome the difficulties of handling actual materials that have been irradiated in nuclear plants, we simulated the production of helium by implanting it in B_4C pellets (collected from hot pressed boron carbide from CEA records) at different temperatures, energies and fluences. Subsequent thermal annealing treatments allowed us to determine the influence of the temperature on the behaviour of the gas in the material. The studies are then carried out using two techniques for investigation:

- determination of the helium diffusion coefficient by Nuclear Reaction Analysis (NRA);
- observation of helium clusters by Transmission Electron Microscopy (TEM).

2.1 Diffusion coefficient determination

The principle of this experiment is to implant ^3He as a surrogate of ^4He in B_4C pellets at a known depth, then apply different annealing treatments and then analyse the samples with a nuclear microprobe, from which we observe the evolution of the helium profiles using the $^3\text{He}(\text{d},\text{p})^4\text{He}$ reaction as a final step. The helium profiles were obtained from the proton energy profiles measured by the detector [18].

To proceed, helium-3 was implanted at room temperature at an energy of 3 MeV to obtain a profile with a projected ion range $R_p \sim 9 \mu\text{m}$ and $\Delta R_p \sim 120 \text{ nm}$ (as given by SRIM [19] calculations). The chosen fluence was 10^{15} at/cm^2 (about $4 \times 10^{19} \text{ at/cm}^3$ at R_p), which was high enough for detecting helium, while expected to remain low enough to avoid the formation of helium clusters. Annealing treatments were carried out between 15 min and 2 h at 900°C and 1 h between 500 and 1000°C in 100°C steps. This temperature range corresponds to the temperatures that the material is exposed to in a fast breeder reactor.

The $^3\text{He}(\text{d},\text{p})^4\text{He}$ NRA measurements were performed using the nuclear microprobe facility of the *Laboratoire d'Étude des Éléments Légers* in CEA Saclay (CEA/DSM/IRAMIS/LEEL). It is a 3.75 MeV single-ended Van de Graaff accelerator, which can supply proton, deuteron, helium-3 and helium-4 ion beams in the energy range from 400 keV to 3.75 MeV (further descriptions of the facility can be found in Ref. [20]).

Based on SRIM calculations (Fig. 5), a 1300 keV energy for the deuterons was chosen with a 5 nA flux and a $50 \times 50 \mu\text{m}^2$ beam spot, which is large enough to mask channelling effects (average grain size of $5 \mu\text{m}$). The energy of the deuterons was chosen in order to have the best yield for the (d,p) reaction cross-section. An absorber foil ($123 \mu\text{m}$ thick Mylar foil) was placed in front of the annular detector, in order to stop the backscattered deuterons and slow down the 19 MeV protons, in order for them to stop in the Si

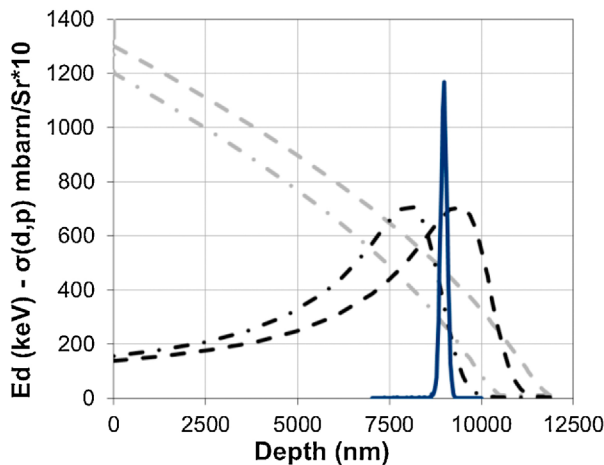


Fig. 5. Calculations for the choice of the energy of the deuterons (between 1200 keV: - - - and 1300 keV: - -) for the (d,p) reaction. Grey: energy of the deuterons versus depth into the material, from SRIM [19]. Black: cross-sections curves according to the initial deuterons energy and along the depth in the material. Blue solid line: implantation profile of helium-3 at 3 MeV in B_4C .

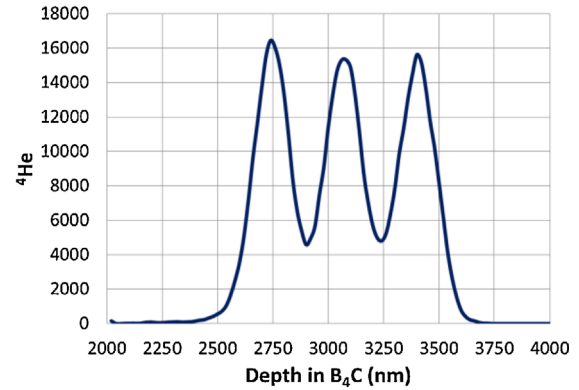


Fig. 6. Helium implantation in B_4C given by SRIM [19]: ^4He , 2.8–2.9–3.0 MeV, $1.5 \times 10^{16} \text{ at/cm}^2$ with a $6 \mu\text{m}$ thick aluminium foil placed in front of the sample.

detector. The obtained proton energy profiles were then converted to helium depth profiles, this allowed an analysis of their evolution and thus enabled us to deduce the apparent helium diffusion coefficient in boron carbide.

2.2 Helium clusters observations

The purpose of this experiment is to observe directly the behaviour of helium (formation of clusters, migration . . .) using Transmission Electron Microscopy (TEM). Helium was implanted in B_4C pellets along a known profile, and annealing treatments were then performed.

To proceed, we implanted helium-4 at 500°C at three different energies (2.8–2.9–3.0 MeV) to get a wider helium distribution. To move the implantation distribution peak closer to the surface, which is required for the preparation of the samples by the focused ion beam (FIB) method, a $6 \mu\text{m}$ aluminium foil was set in front of the sample. This setup led to a helium distribution between 2.65 and $3.55 \mu\text{m}$ from the surface of the pellet (from SRIM calculations, as shown in Fig. 6). We used a fluence of $1.5 \times 10^{16} \text{ at/cm}^2$, leading to a maximum helium concentration of about 10^{21} cm^{-3} , high enough to allow the formation of bubbles. Subsequent annealing treatments were performed in the temperature range of $900\text{--}1500^\circ\text{C}$.

The thin-foil specimens were prepared by FIB: classical electrolytic methods cannot be used here, and due to B_4C brittleness, small samples are required. The samples are then about $8 \mu\text{m}$ large, $6 \mu\text{m}$ deep and 200 nm thick. TEM observations were performed at the *Service de Recherches Métallurgiques Appliquées* in CEA Saclay (DMN/SRMA/LA2M) on a Jeol 2010F with a Field Emission Gun (FEG) and on a Jeol 2100, both operating at a 200 kV voltage.

3 Results

3.1 Helium diffusion coefficient determination

The helium profiles obtained by NRA were assumed to be Gaussian for simplicity. In that case, the theory of the

diffusion in the grain (pure diffusion, single mechanism, without any formation of clusters) gives:

$$\sigma_T^2 = \sigma_0^2 + 2 \cdot D_T \cdot t, \quad (1)$$

where σ_T is the standard deviation obtained after an annealing treatment of duration t at the absolute temperature T , σ_0 the standard deviation before annealing and D_T , the diffusion at temperature T defined by:

$$D_T = D_0 \cdot \exp\left(-\frac{E_a}{kT}\right), \quad (2)$$

with D_0 , the pre-exponential factor, E_a , the activation energy and k , the Boltzmann constant (8.617×10^{-5} eV/K).

To reach the D_0 and E_a values, we have to measure the standard deviation of the Gaussian profiles, then use equation (1) to find D_T . If the D_T values are aligned in an Arrhenius diagram ($\log(D_T)$ vs. $1/T$), then the D_0 and E_a values can be deduced.

The experimental NRA spectra were given in channels as a function of a number of counts. To convert channels into depth, we evaluated the depth at which helium had been implanted by using the SRIM profiles, from which we deduced a linear channel-depth conversion. This approximate conversion can then be used to perform preliminary evaluations of the diffusion coefficients. More accurate calculations taking into account the full setup design [18] are in progress.

We proceeded to carry out two annealing sessions: one at different temperatures over 1 h to draw the Arrhenius diagram, and another at 900 °C from 15 min to 2 h. The latter then allowed a better estimation of the diffusion coefficient at 900 °C for the Arrhenius diagram.

Because of a low statistic (around 300 events for a profile), complex helium profiles cannot be observed and we assumed Gaussian profiles. Some of the results obtained from the one-hour annealing process are plotted in Figure 7.

As shown in Figure 7, the profiles broadened after annealing. We also observed that the area of the profiles was constant (by integration of the curves). This shows

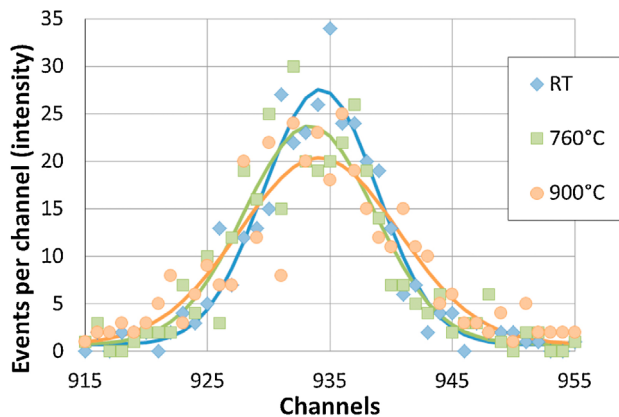


Fig. 7. Gaussian fitting (solid lines) of the ^3He profiles in B_4C analysed by NRA with deuteron energy of 1300 keV. Samples were annealed over 1 h at different temperatures (°C) before the analysis.

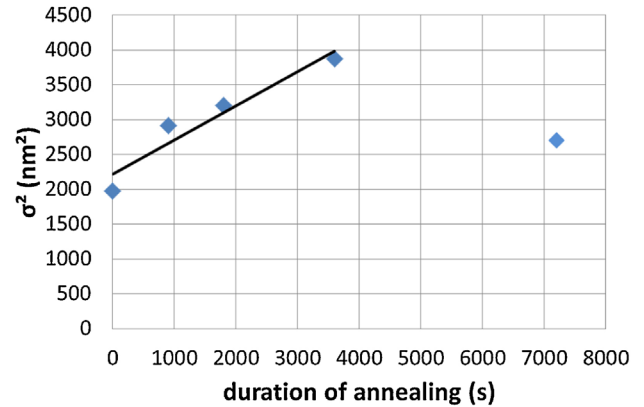


Fig. 8. ^3He profiles in B_4C analysed by NRA with deuteron energy of 1300 keV. Samples were annealed at 900 °C for different durations (s) before the analysis.

that diffusion occurred in the material without loss of helium: these two points are required in order to calculate a diffusion coefficient.

The 1000 °C curve was not shown in Figure 7 because its width was narrowed and its intensity reduced as compared to the 900 °C curve. It may imply that a part of helium not only diffused on long distances, with concentrations lower than the detection limit of the experiment, but also formed clusters close to the implanted zone. Thus, this data point was not taken into consideration in the Arrhenius diagram.

The profiles obtained from the annealing experiments at 900 °C during different durations (Fig. 8) also broadened after annealing. From 15 min to 1 h, the broadening is quite monotonous so it allowed us to obtain better accuracy for the value of D_T at 900 °C for the Arrhenius diagram. But the sample annealed for 2 h had a profile similar to the one observed after the annealing at 1000 °C: the apparent width and the intensity decreased, so it was not taken into consideration in the Arrhenius diagram.

Afterward, we inserted all the values of the isochronal annealing up to 900 °C in an Arrhenius diagram (Fig. 9) and

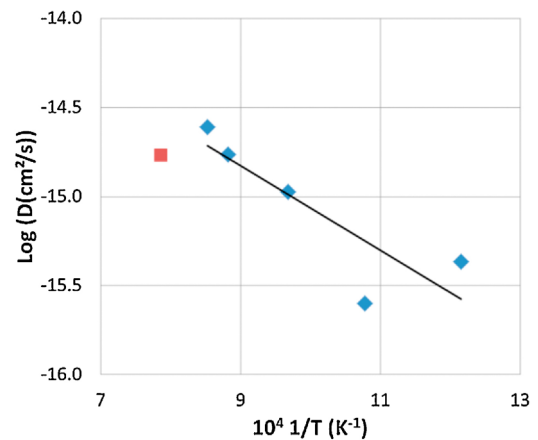


Fig. 9. Arrhenius diagram of the diffusion coefficient of ^3He in B_4C . The 1000 °C point (in red) was excluded for the linear fitting.

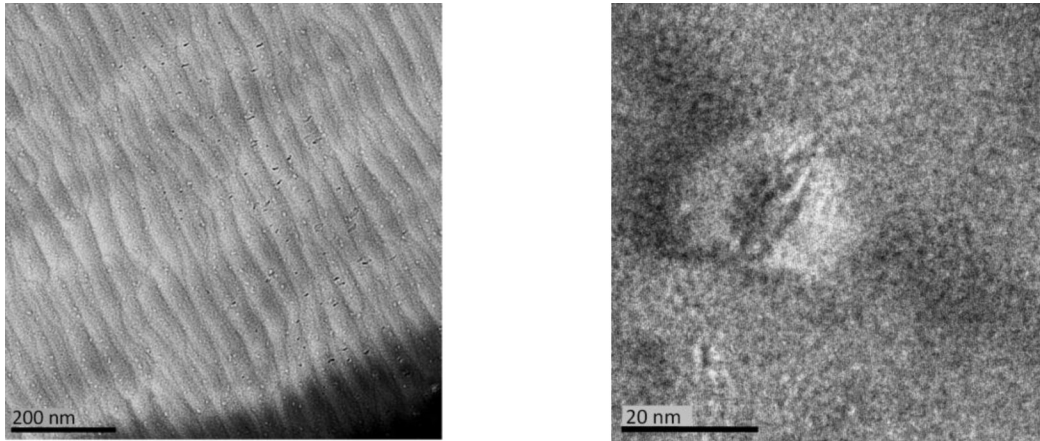


Fig. 10. ^4He implanted in B_4C then annealed at 900°C . Left: intra-granular bubbles band (in black, the bubbles; riddles and white dots are artefacts due to FIB thinning). Right: strain field around a bubble.

the data point at 900°C resulted from the analysis of the isothermal annealing except the 2 h data.

As shown in Figure 9, the helium profiles which have the same intensity (Fig. 7: from RT to 900°C included) are correctly aligned in the Arrhenius diagram. This shows that parameters fitting to a diffusion law can be estimated. From a linear fitting, we deduced:

- $D_0 = 1.19 \times 10^{-12} \text{ cm}^2/\text{s}$;
- $E_a = 0.523 \pm 0.107 \text{ eV/atom}$.

3.2 Helium clusters observations

For the TEM observations, all the samples were implanted at the same fluence ($1.5 \times 10^{16} \text{ at}/\text{cm}^2$) at 500°C , and then annealed at different temperatures.

For the as-irradiated sample, no clusters were observed. Helium clusters may have nucleated but these were then too small to be observed (only a few atoms).

For the 900°C annealed sample (Fig. 10), a bubble band was observed. Surprisingly, the band was only 400 nm wide (instead of a $1 \mu\text{m}$ wide band, as shown in Fig. 6). Clusters

were very small (between 3 and 20 nm). The smallest clusters were ellipsoidal. The larger bubbles tended to grow in a flat shape and be orientated in parallel. It was difficult to orientate those flat bubbles with respect to the crystal structure, because they need to be on the edge for the observation (which is not exactly the case here), and the sample could not be correctly oriented because the sample was too far from a zone axis. We can notice the presence of strain fields around the clusters as a pattern of “butterfly’s wings”, which was a consequence of the high pressure of the gas inside the cluster [13].

For the 1100°C annealed sample (Fig. 11), the same band was observable. However, in this case, all bubbles were plate-like and parallel to each other, showing that strong orientation constraints were acting in the material. As they were on the edge, it became possible to find their habit plane. Two methods can be used: either by recording a diffraction pattern then indexing it, or performing high resolution observations by measuring the distance between atomic planes then deducing their Miller indexes. Both methods led to the same result: the bubbles were oriented along the (111) rhombohedral plane (or (0003) hexagonal plane), as was already reported in literature [10–13].

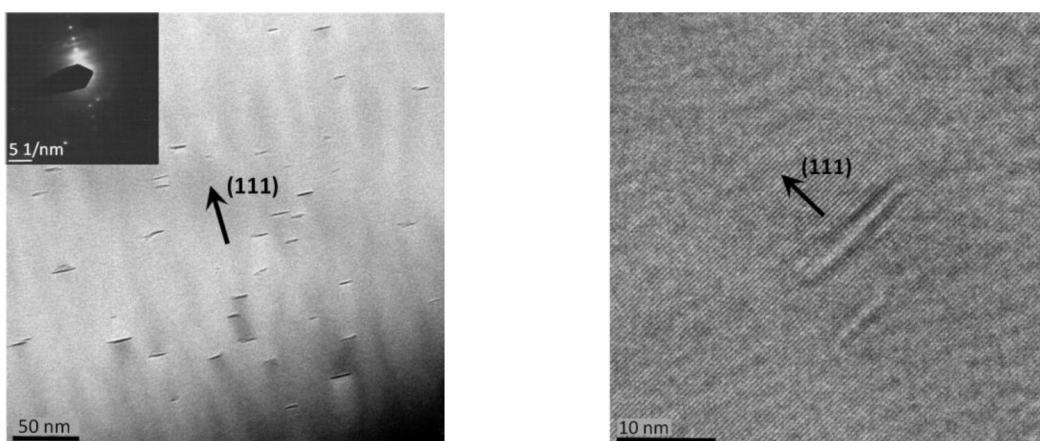


Fig. 11. ^4He implanted in B_4C then annealed at 1100°C . Left: parallel plate-like intra-granular bubbles band with strain fields and the corresponding diffraction pattern. Right: two oriented bubbles in high resolution observation.

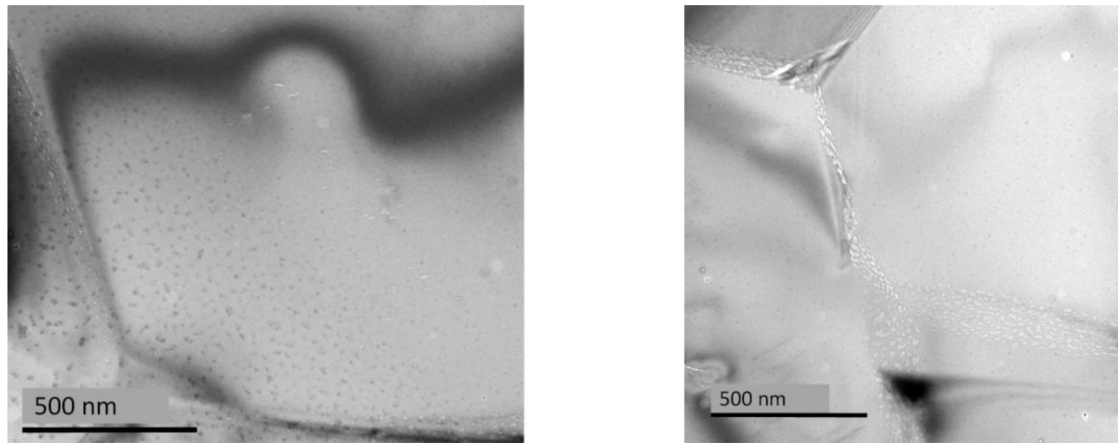


Fig. 12. ^4He implanted in B_4C and annealed at $1300\text{ }^\circ\text{C}$. Left: intra-granular plate-like bubbles and inter-granular bubbles (bubbles appear in white; the black spots are artefacts due to FIB preparation). Right: inter-granular bubbles (two triple points).

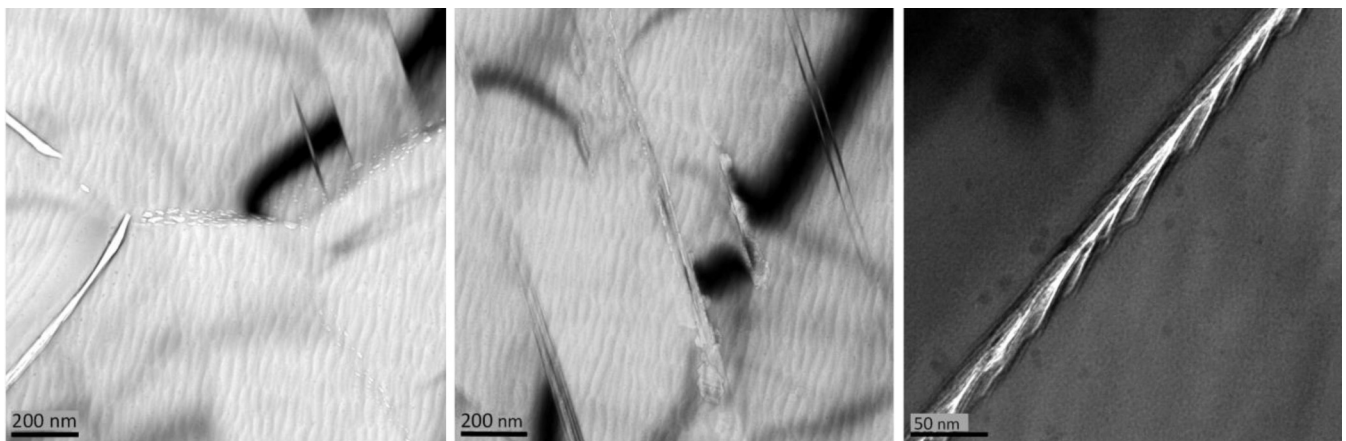


Fig. 13. ^4He implanted in B_4C and annealed at $1500\text{ }^\circ\text{C}$. Left: two triple points. Helium was trapped in the grain boundaries in the form of bubbles, or the grain boundaries are opened. Middle: helium bubbles located at twin boundaries (riddles due to FIB thinning). Right: opened grain boundaries with a shape of “stair steps”.

For the $1300\text{ }^\circ\text{C}$ annealed sample (Fig. 12), we can notice a different helium behaviour. The flat parallel bubbles band was still visible, and close to the centre of the maximum calculated by SRIM, but only a few bubbles are present. Large quantities of helium have diffused through long distances in the grain boundaries where bubbles were also formed. Instead of having a $1\text{ }\mu\text{m}$ large profile at around $3\text{ }\mu\text{m}$ from the surface (according to SRIM), bubbles were found between 0.5 and $4.2\text{ }\mu\text{m}$ from the surface, most of them in the grain boundaries. Also, it was noticed that most of the helium bubbles were found between the surface, and the original maximum of the helium distribution, rather than beyond the implantation peak. Different mechanisms were thus activated between $1100\text{ }^\circ\text{C}$ and $1300\text{ }^\circ\text{C}$.

For the $1500\text{ }^\circ\text{C}$ annealed sample (Fig. 13), the behaviour of helium is different again, and may be due to the specific temperature of $1500\text{ }^\circ\text{C}$, which is close to the brittle-plastic transition of boron carbide [2]. No helium bubbles were observed in the grains, except in some defects such as twin boundaries, which are typical defects in boron carbide. All visible helium was observed as bubbles with

various shapes in the grain boundaries, over distances much longer than the peak width calculated by SRIM. No bubbles were observed in the grains. Some grain boundaries were opened in front of the implantation maximum. As was noted for the B_4C annealed at $1300\text{ }^\circ\text{C}$, instead of having a $1\text{ }\mu\text{m}$ large helium band at about $3\text{ }\mu\text{m}$ depth, a much larger band, that is at 0.4 to $5.3\text{ }\mu\text{m}$ from the surface was observed. When observed at high resolution, we noticed that the opened grain boundaries have a shape of “stair steps”.

4 Discussion

4.1 Diffusion coefficient determination

When annealed for 1 h at a temperature lower than $700\text{ }^\circ\text{C}$, helium did not diffuse significantly, so the microprobe’s depth resolution may not be sharp enough to detect profile broadening. That was why the $550\text{ }^\circ\text{C}$ and the $655\text{ }^\circ\text{C}$ data points were so far apart from the linear fitted line in the Arrhenius diagram. This dispersion allowed us to estimate

the error inherent in the value of the activation energy that we have measured.

The helium profile in the B_4C sample annealed at $1000^\circ C$ had narrowed, and its intensity had lowered, showing that helium was not diffusing progressively anymore. This may be due to the conjunction of the formation of clusters in the implanted slab, and long-range diffusion up to and in the grain boundaries. In that case, due to the low yield of the method, the foot of the profile would be too low to be detected, thus leading to an underestimation of the integral intensity of the peak. For example, we have observed on the TEM images that bubbles would appear around $900^\circ C$, but at higher fluences. It could then be assumed that at $1000^\circ C$ (with smaller fluences), helium clusters can also nucleate and affect the intra-granular diffusion. The same behaviour was observed for the sample annealed at $900^\circ C$ for 2 h, for which the helium profile had a similar width as the sample annealed at $1000^\circ C$, showing that there were specific annealing temperature and duration thresholds above which intra-granular diffusion was affected by other mechanisms: influence of grain boundaries and formation of clusters.

In order to check the obtained value of the diffusion coefficient, we compared it to the diffusion coefficient of helium in SiC [21], which is a ceramic with properties similar to boron carbide: they both are built with light elements with tight covalent bonding. Moreover, the two materials were prepared by powder sintering in our investigations. We observed (Fig. 14) similar diffusion coefficients for the two compounds.

One problem of this method is the low number of data points, which prevented an accurate analysis of the profiles that would be necessary to observe asymmetric or long-range diffusion: in fact, only a standard deviation and an integral intensity can be evaluated. Indeed, Gaussian fits were based on only a few points, due to the low dose of helium-3 in the samples, and the deep implantation, the small flux of the accelerator and the few hours of experiment to analyse the samples. To get more accurate results, more data points that will contribute to better statistical power of the analysis are needed.

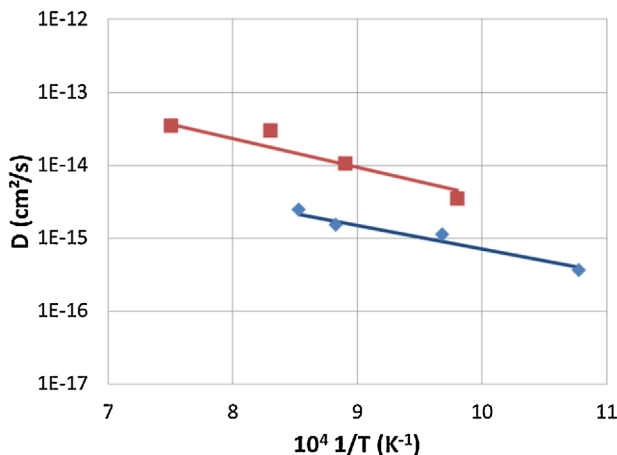


Fig. 14. Comparison of Arrhenius diagrams for the diffusion of helium in B_4C (in blue) and SiC [21] (in red).

4.2 Helium clusters observations

Inside a fast breeder reactor, B_4C is exposed to a temperature range of $500\text{--}1200^\circ C$ in normal conditions. The TEM observations gave a good scope of the behaviour of helium in B_4C according to the annealing temperature. The gas was found in different forms:

- $500^\circ C$: bubbles were not formed yet;
- $900^\circ C$: bubbles appeared. They were circular and small, and some of them began to orientate parallel to each other;
- $1100^\circ C$: bubbles were all plate-like and parallel in the (111) rhombohedral plane;
- $1300^\circ C$: a few intra-granular plate-like parallel bubbles were observed, and most of helium had diffused in the grain boundaries over large distances. This long-range diffusion appeared asymmetric, since bubbles were mainly observed in front of the implanted zone. This point should be addressed. In particular, the influence of material damage (here produced by helium slowing down) should be analysed;
- $1500^\circ C$: brittle-plastic transition temperature of B_4C . Helium was observed in the grain boundaries over long distances in the form of bubbles with different shapes, or was trapped in structural defects such as twin boundaries or dislocations. The same asymmetric distribution as after annealing at $1300^\circ C$ is observed. Some of the grain boundaries were even opened.

Only the sample annealed at $1100^\circ C$ had a correct orientation to allow determination of the orientation of the parallel bubbles in the crystal. We found that they all were parallel to the (111) rhombohedral plane. The orientation of the grains in the other samples did not allow us to obtain unambiguous orientations to perform such an analysis.

The results we obtained here were coherent with previous ones [10–15]. However, implanting helium in a thin slab led to different behaviours as compared to those observed in homogeneously implanted or neutron irradiated materials. In particular, there is evidence for long range, to distances much larger than the ones that could be deduced from the diffusion coefficient we obtained. This showed that different mechanisms were competing in the material, such as nucleation of clusters and diffusion, leading to quite different defects (bubbles) distributions. Such complex behaviours should be further analysed. Intra-granular micro-cracks were not observed. This was consistent with previous observations [4], showing that cracking occurs only for a higher helium concentration, around 5×10^{21} at/cm³.

5 Conclusion

The tests we conducted here gave preliminary results that can be used to guide further studies about the behaviour of helium implanted in boron carbide B_4C . To simulate the production of helium that occurs in a nuclear reactor, we implanted helium in the samples and proceeded to thermal annealing to observe and analyse the diffusion of the gas in the material.

Helium-3 was implanted in small quantities in B₄C. Then the samples were annealed at different temperatures and analysed with a nuclear microprobe by NRA (Nuclear Reaction Analysis). The implantation profiles broadened with an increase in temperature. At low temperatures, the degree of diffusion was lower than the microprobe sensitivity limit. Then up to 900 °C, the gas diffused significantly, at 1000 °C, helium partly escaped to the grain boundaries and possibly began to form clusters. From those results, a diffusion coefficient was deduced ($E_a = 0.52 \pm 0.11$ eV/atom), which was close to the equivalent coefficient of diffusion of helium in SiC.

Helium-4 in larger quantities was implanted at 500 °C in B₄C. Then the samples were annealed until 1500 °C and thinned by FIB to be observed by TEM (Transmission Electron Microscope). At 500 °C, helium clusters were not observable. At 900 °C, helium started to accumulate as pressurised bubbles. Then at 1100 °C, the bubbles were flat, all parallel to each other and oriented along the (111) rhombohedral planes. At 1300 °C, long distance diffusion in grain boundaries occurred and only a few intra-granular bubbles were visible. At 1500 °C, helium was found only in the grain boundaries in the form of bubbles and some parts of the grain boundaries were opened.

We are highly grateful to Benoit Arnal (CEA Saclay, DEN/DMN) who prepared the TEM thin-foil samples.

References

1. V. Dornich et al., J. Am. Ceram. Soc. **94–11**, 3605 (2011)
2. F. Thevenot, J. Eur. Ceram. Soc. **6**, 205 (1990)
3. H. Werheit et al., J. Phys.: Condens. Matter **24**, 305 (2012)
4. D. Gosset, Neutron absorber materials, in *Handbook of nuclear engineering* (Dan Gabriel Cacuci ed., 2010)
5. ENDF database, www-nds.iaea.org/exfor/endl.htm
6. DOE Fundamentals Handbook, *Nuclear physics and reactor theory* (DOE-HDBK-1019/1–93, 1993)
7. K.N. Kushita et al., Microsc. Microanal. Microstruct. **6**, 149 (1995)
8. T. Maruyama et al., Effects of radiation on materials, in *21st International Symposium ASTM STP1447, 2004* (2004), p. 670
9. D. Gosset et al., to be published in NIM-B (2015)
10. G.L. Copeland, J. Nucl. Mater. **43**, 126 (1972)
11. T. Maruyama et al., J. Nucl. Mater. **133&134**, 727 (1985)
12. A. Jostsons et al., J. Nucl. Mater. **44**, 91 (1972)
13. T. Stoto et al., Radiat. Eff. **105**, 17 (1987)
14. V.P. Tarasikov, Atom. Energy **106**, 220 (2009)
15. W.V. Cummings et al., T. Am. Nucl. Soc. **15**, 742 (1972)
16. K. Froment et al., J. Nucl. Mater. **188**, 185 (1992)
17. H. Suzuki et al., J. Nucl. Sci. Technol. **16**, 588 (1979)
18. D. Gosset et al., J. Nucl. Mater. **303**, 115 (2002)
19. J.F. Ziegler, www.srim.org
20. P. Trocellier, Microsc. Microanal. Microstruct. **7**, 235 (1996)
21. Y. Pramono et al., J. Nucl. Sci. Technol. **41**, 751 (2004)

Cite this article as: Vianney Motte, Dominique Gosset, Sandrine Miro, Sylvie Doriot, Suzy Surblé, Nathalie Moncoffre, Helium behaviour in implanted boron carbide, EPJ Nuclear Sci. Technol. 1, 16 (2015)